Geophysical Prospecting

ORIGINAL ARTICLE OPEN ACCESS

3D Inversion of Radiomagnetotelluric Data From the Sub-Himalayan Fault Zone, India—Combining Scalar, Tensor and Tipper Transfer Functions

Burak F. Göçer[1] | Wiebke Mörbe[1,2] | Bülent Tezkan[1] | Mohammad Israil[3] | Pritam Yogeshwar[1,2]

[1]Institute of Geophysics and Meteorology, University of Cologne, Cologne, Germany | [2]LIAG Institute for Applied Geophysics, Hanover, Germany | [3]Department of Earth Sciences, Indian Institute of Technology Roorkee, Roorkee, India

Correspondence: Pritam Yogeshwar (pritam.yogeshwar@liag-institut.de)

Received: 24 January 2025 | **Accepted:** 11 July 2025

Funding: This work was conducted as part of the INDO-GERMAN joint research collaboration under the DST-DAAD project (Project No. DST/INT/DAAD/P-19/2019 - TPN 73918; DAAD No. 57622770). We gratefully acknowledge the financial support provided by the funding agencies (DST and DAAD).

Keywords: 3D inversion | electromagnetics | Himalaya | radiomagnetotellurics | tensor processing | tipper

ABSTRACT

Radiomagnetotellurics (RMTs) is an efficient frequency-domain electromagnetic technique for mapping subsurface electrical resistivity, particularly suited for near-surface investigations. This method utilizes commonly available civil and military radio transmitters, broadcasting between 10 kHz and 1 MHz, as sources to measure electric and magnetic field responses at the surface. Modern RMT receiver systems comprise five components (two electrical antennas and three magnetic coils), allowing for the estimation of the full impedance tensor and the tipper transfer function for the vertical magnetic field. In this study, RMT data were acquired to investigate the shallow structure of the Himalayan Frontal Thrust (HFT) fault in the Sub-Himalayan region around Uttarakhand, India. Data were collected at 312 stations along eight profiles over an area of roughly 500 m × 70 m. The dense station distribution enables a 3D inversion of the dataset in the extended frequency range of up to 1 MHz. The observed data were processed using scalar as well as tensor estimations to obtain full impedances and tipper transfer function. We integrated scalar-estimated data from zones with an approximately 2D conductivity distribution in the full-tensor dataset. This approach ensured robust 3D modelling during the initial RMT inversion performed with the ModEM algorithm. To date, a joint 3D interpretation of RMT full impedance tensor and tipper transfer function has not yet been reported. Furthermore, the near-surface manifestations of the HFT have not previously been explored by RMT. The derived 3D model from combined scalar, tensor and tipper data reveals a conductivity contrast zone that aligns well with the HFT fault outcrop and complementary geological information. The derived geo-electrical structure recovers the local sediment thickness and shallow fault inclination.

1 | Introduction

Ground-based geophysical inductive electromagnetic (EM) methods are based on the principle of the measurements of temporal variations of electric and magnetic fields. These techniques can be classified as passive or active, using either natural or artificial sources. As a modification of the passive magnetotelluric (MT) method towards high frequencies, civil and military radio transmitters serve as sources for the radiomagnetotelluric (RMT) technique (Tezkan 2009). Due to the limited frequency range

between 10 kHz and 1 MHz, the RMT method is mainly applicable for shallow investigations down to a few hundred of meters, yet depending on the subsurface electrical conductivity structure as well as available signals from radio transmitters. Various hydrogeological, environmental, engineering and resource exploration studies demonstrate the wide applicability of using RMT for efficiently imaging the earth's subsurface (e.g., Turberg et al. 1994; Tezkan et al. 2000; Bastani and Pedersen 2001). Although MT is mainly used for deep studies (e.g., Unsworth et al. 2005), tracking shallow fault manifestations is an integral part for understanding such systems across multiple depth and spatial scales (Bastani et al. 2011).

Amongst EM studies, several RMT case histories exist that investigate fault zones (Candansayar and Tezkan 2008; Bastani et al. 2011; Malehmir et al. 2016; Widodo and Tezkan 2015; Tezkan et al. 2019). Due to a limited applicability of RMT in remote areas where signal availability can be scarce and due to a limited penetration depth, recent developments promote the utilization of controlled sources extending the frequency range below 10 kHz (e.g., Saraev et al. 2017; Tezkan et al. 2019; Smirnova et al. 2023).

Nowadays, deep MT data are commonly interpreted in three dimensions, allowing for imaging complex subsurface structures, mainly due to computational advancements (e.g., Farquharson et al. 2002; Grayver 2015). However, 3D inversion examples using RMT data, especially in the extended frequency range up to 1 MHz, are scarce in the geophysical literature. The early work of Newman et al. (2003) first use 3D inversion of scalar RMT data to image a waste site in Germany. A 3D inversion of full tensor RMT data was presented by Bastani et al. (2012). Recently, Fadavi Asghari et al. (2023) presented the first 3D controlled source and RMT inversion study focusing on impedance evaluation using the modular electromagnetic (ModEM) inversion algorithm, developed by Egbert and Kelbert (2012) and widely applied to deep MT studies.

In this article, we present a sophisticated 3D inversion study using the well-established ModEM software package to interpret RMT data from the Himalayan Frontal Thrust (HFT) fault zone in northern India. The HFT, representing the youngest thrust zone, is considered a potentially active fault with the likelihood of future rupture due to strain accumulation (Rajendran et al. 2015). Consequently, it has been the focus for extensive deep geophysical studies (Israil et al. 2008; Miglani et al. 2014). To date there are no shallow RMT studies that trace near-surface manifestations of the HFT. Besides, there are only few RMT studies demonstrating the applicability of the RMT method for the Indian subcontinent (Yogeshwar et al. 2012; Devi et al. 2020). Furthermore, due to limitations in source signal availability as well as limited signal quality, RMT studies incorporating full impedance tensor estimations as well as tipper data are not yet reported. We provide a comparative analysis of scalar and tensor processing and propose a strategy to combine both datasets. Subsequently, we combine tensor, scalar and tipper RMT data and run 3D inversion on the full combined datasets. We evaluate the derived 3D model in terms of visual consistency as well as geological plausibility.

2 | Geological Setting and Survey Design

The study area is located in the Sub-Himalayan zone near Dehradun, Uttarakhand, India (Figure 1a). The Himalayan orogenic belt formed approximately 50 million years ago due to the collision between the Indian and South Eurasian plates. Geologically, the Himalayas are divided into three segments, running from south to north: the Sub-Himalayan, Lesser Himalayan and Higher Himalayan zones. Horizontal extrusion, crustal shortening and lithospheric delamination observed in the region result from the horizontal movement of rock masses along the north-dipping thrust planes (Le Fort 1975; Molnar 1990). The area features a series of regional thrust systems, created by the crustal shortening along the northern margin of the Indian Plate (Valdiya 1973; Verma 1974). Figure 1b shows a block diagram and schematic cross-section of the Uttarakhand Himalayan region, highlighting the main thrusts, listed from north to south as the Main Central Thrust (MCT), Main Boundary Thrust (MBT) and HFT (Thakur and Pandey 2004). The Sub-Himalayan region, located between the MBT and HFT (see Figure 1a,b), is composed of Paleocene–Lower Eocene marine sediments, the Oligocene Dharamsala/Muree formation, and the Middle Miocene-Pleistocene fluviatile Siwalik Group (Yeats and Thakur 2008).

The primary focus of this research is on the HFT and its shallow characteristics. The HFT reveals a series of deformation structures in the Sub-Himalayan region, where an active, southward-propagating fold-thrust system has driven longitudinal expansion (Kumar et al. 2010). Known as the Siwalik range, the Sub-Himalayan region abuts the Indo-Gangetic plain, where an abrupt physiographic fracture delineates the HFT. The HFT's southern edge includes coalescing fans from the Siwalik range, forming an uplifted piedmont zone, spanning 15–20 km (Thakur and Pandey 2004). Characterized by large active anticlines, the Siwalik range has developed fault-propagation and fault-bending folds in the HFT's hanging wall (Thakur 2013). The Siwalik Group is divided into Lower, Middle and Upper Siwaliks with ages from 14 to 0.5 Ma.

Wesnousky et al. (1999) studied the higher terrace deposits (F1 in Figure 1d) in the Siwalik Hills, which are uplifted 20–30 m above stream level due to HFT displacement. The exposed outcrops in Figure 1c show fluvial terraces with a thin soil layer overlying loamy sand and a 2–3 m layer of pebble cobble. In contrast, the lower terrace (F3) is only slightly uplifted. The Solani River cuts through the Siwalik foothills, composed of Mio-Pliocene-age pebbles, boulders and sandstone. The surveyed area in the streambed exhibits no topographic variations along the aligned profiles. It is covered by alluvial deposits (F2 in Figure 1d) of fine sand, coarse gravel and partly mudstone.

Early studies in the Mohand area assumed the HFT to be a blind thrust, hidden beneath surface deposits (Raiverman et al. 1990). However, trench studies show that the HFT reaches the surface, previously obscured by thin deposits in active streambeds (Kumar et al. 2006). Srivastava et al. (2016) observed a 700 m fault core and surrounding damage zone in the survey area. The fault core,

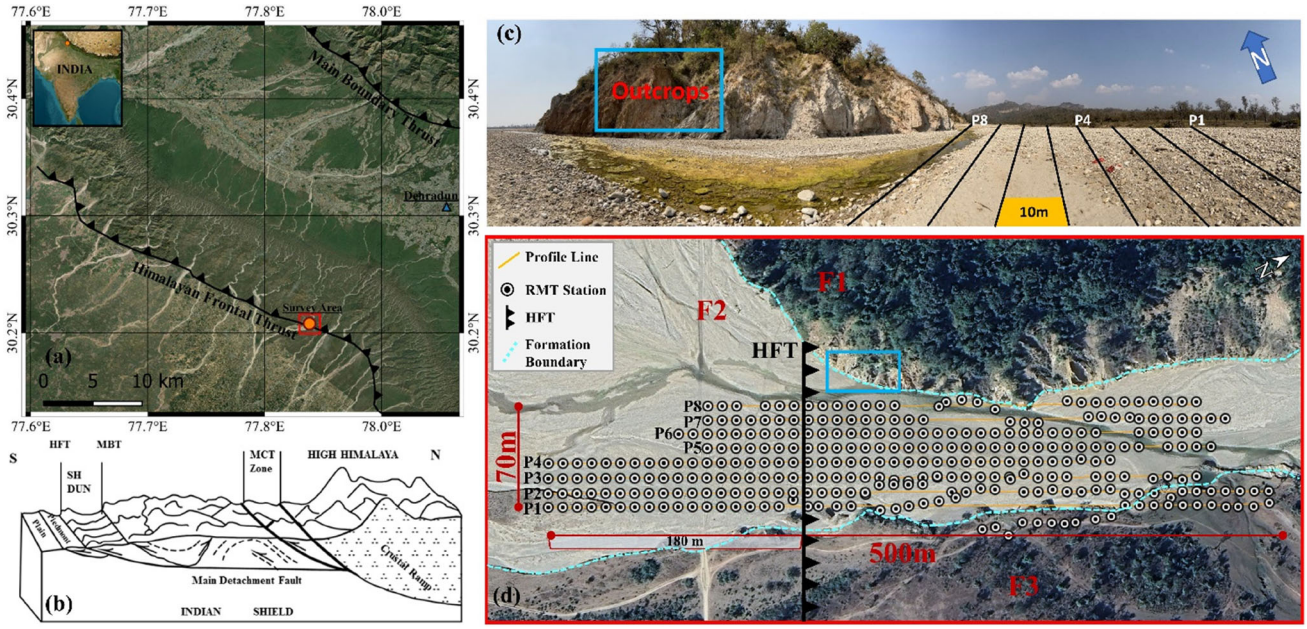

FIGURE 1 | (a) Map of the study area (marked as red box) near Mohand, Uttarakhand. The HFT and MBT faults are indicated as black line. (b) A block diagram of the Himalayan region (Thakur and Pandey 2004). (c) Image of the uplifted outcrops (blue box) and the RMT profiles (black lines). (d) Location of RMT stations (black circles) organized into eight profiles, numbered from P1 to P8. Turquoise dashed lines along the river bed show the boundary of different geological formations (F1–F3): F1 refers to the higher terrace; F2 to the active flood plain; F3 refers to the lower terrace (Wesnousky et al. 1999). HFT, Himalayan Frontal Thrust; MBT, Main Boundary Thrust; MCT, Main Central Thrust.

150–250 m wide, transitions into a hanging wall damage zone rich in fault gouge, forming island-channel structures with highly fractured Middle Siwalik rocks encircled by fine gouge material. This reveals that the HFT may be an emergent fault, exposed by erosion and creating a visible fault trace on the earth's surface.

RMT data acquisition, using the RMT-SM25 system (Tezkan and Saraev 2008), covered eight parallel profiles (P1–P8 in Figure 1d) with 312 stations. The profiles, oriented approximately 26° SSW–NNE, run parallel to visible outcrops bounding the survey area to the north. Profiles and stations were spaced at 10 m intervals, with few gaps due to water coverage. Capacitive electrodes were used to measure electric fields, which is beneficial due to high contact resistance in the area. The survey covered a 500 m × 70 m area with dense station distribution, allowing for subsequent 3D modelling. From a geological perspective, this study aims at (1) resolving the shallow HFT fault zone transition, (2) tracking the outcrops to depth and (3) identifying the shallow fault dipping angle.

3 | Methodology

RMT is a frequency-domain technique for near-surface geophysical exploration. EM waves from distant radio transmitters penetrate the conductive earth, inducing eddy currents and associated time alternating electric and magnetic fields. These fields can be measured at the surface (Figure 2a) with a receiver unit connected to two electric antennas and a triple induction coil. The setup enables estimation of the complete impedance tensor and tipper. Localized radio transmitters in the 10 kHz

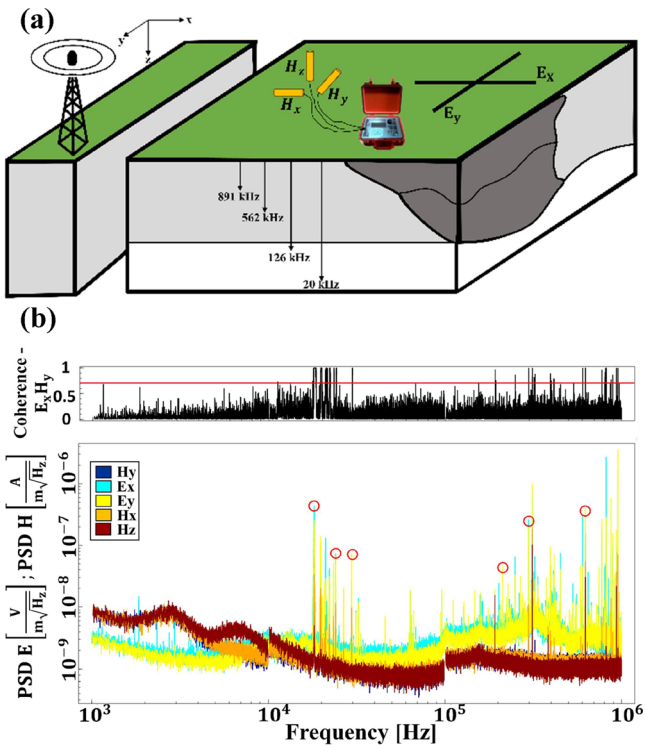

FIGURE 2 | (a) Schematic diagram of the RMT technique. Lower frequencies are associated with greater penetration depths. (b) Power spectral density plot (PSD) of the magnetic and electric field components for an exemplary RMT station together with the coherency of E_x and H_y. The red circles mark transmitter signals with high coherency. *Source*: (a) Modified from Tezkan (1999).

to 1 MHz frequency range (VLF: 10–30 kHz, LF: 30–300 kHz, MF: 300–1000 kHz) create plane-wave conditions, with source-receiver distances far beyond three to five skin depths (Goldstein and Strangway 1975). For typical earth resistivities less than 1000 Ω m and typical RMT frequencies, displacement currents are negligible, enabling a quasi-static diffusion behaviour. RMT is widely used in Europe, where various radio transmitters operate across VLF, LF and MF bands (Pedersen et al. 2006).

The measured electric and magnetic fields are analysed using the complex, frequency-dependent impedance tensor $\underline{\underline{Z}}$ (Cantwell 1960).

$$\overline{E}(\omega) = \underline{\underline{Z}}(\omega)\overline{H}(\omega) \tag{1}$$

$$\underline{\underline{Z}}(\omega) = \begin{pmatrix} Z_{xx}(\omega) & Z_{xy}(\omega) \\ Z_{yx}(\omega) & Z_{yy}(\omega) \end{pmatrix} \tag{2}$$

where $\bar{E}$ and $\bar{H}$ are the electric and magnetic fields; the subscripts x and y represent horizontal measurements directions; and the angular frequency $\omega = 2\pi f$. In an idealized 2D scenario, where the geological strike aligns with the x-axis, the conservation of current across conductivity boundaries leads to the decoupling of EM fields into two independent polarizations. The off-diagonal impedance tensor components correspond to these polarizations: one involving electric fields parallel to the strike, referred to as E-polarization (Z_{xy}), and the other involving magnetic fields parallel to the strike, referred to as B-polarization (Z_{yx}). However, in a 3D conductivity distribution, this mode separation is no longer applicable. Following this approach, the frequency-dependent apparent resistivity (Equation 3) and phase (Equation 4) are derived from the impedance tensor, as described by Cagniard (1953):

$$\rho_{a_{ij}} = \frac{1}{\mu_0 \omega} \left| Z_{ij} \right|^2 \tag{3}$$

$$\Phi_{ij} = \tan^{-1}\left[\frac{I(Z_{ij})}{R(Z_{ij})}\right] \quad i,j = \{x,y\} \tag{4}$$

Another important linear relationship in EM field analysis is described by the vertical magnetic transfer functions (TFs) or tipper vectors. These relate the vertical magnetic field component (H_z) to the horizontal magnetic components (H_x, H_y) in a vector form (Vozoff 1972). To evaluate the tipper elements (T_x, T_y), the vertical magnetic field component must be measured:

$$H_z = \begin{pmatrix} T_x & T_y \end{pmatrix} \begin{pmatrix} H_x \\ H_y \end{pmatrix} \tag{5}$$

If lateral variations in subsurface conductivity exist on spatial scales comparable to or exceeding the penetration depth of the induced horizontal magnetic fields, these variations produce a vertical magnetic field component.

3.1 | Data Processing

Sophisticated processing routines are required to estimate the TFs, impedance tensor Z and tipper vector $\mathbf{T}$ from the time series of the recorded electric and magnetic field components. We use the EMP algorithm (Shlykov 2018), specifically developed for the RMT-SM25 system, implementing robust and well tested processing routines (Bastani and Pedersen 2001; Egbert and Booker 1986). A fast Fourier transform (FFT) is applied to compute auto- and cross-spectra. The coherency describes the linear correlation between the perpendicular electric and magnetic field components with values between 0 and 1. This serves as a measure of signal quality. Lower coherence values indicate noisy signal. To mitigate noisy TFs, a coherence threshold is set. The auto-spectra for each recorded field component at an exemplary RMT station are shown in Figure 2b. Usable transmitter signals in the range of 18 kHz to 1 MHz with high signal-to-noise (S/N) level are marked. As radio transmitters are located in various directions, emitted signals are recorded with a certain azimuth angle at the RMT station. The azimuth angle is calculated with respect to the profile direction, assuming fields are recorded perpendicular and in-line. Only radio transmitters within a specified azimuth range are considered for processing. The chosen range typically varies depending on the survey region, as the direction and signal strength of transmitters can differ. To ensure sufficient signals for data analysis, a certain azimuth range is required. Azimuth ranges of ±15° and ±30° have commonly been utilized in the literature (e.g., Tezkan and Saraev 2008; Saraev et al. 2017; Fadavi Asghari et al. 2023). The two criteria, coherence threshold and azimuth range, are carefully chosen during RMT data processing to ensure a balance between sufficient signals for evaluation using inversion and discarding noisy data that may lead to false interpretation. Here, we choose a coherency threshold of 0.7 and an azimuth range of ±35°.

The simultaneous measurement of all field components facilitates tensor estimation, allowing the full calculation of auto- and cross-spectra for all components. To estimate tensor TFs, a band-averaging technique is applied, typically within a narrow frequency band of one octave (e.g., Gamble et al. 1979; Pedersen 1982). For the MT method, TFs are commonly estimated using tensor processing routines. However, for RMT the signal spacing between radio transmitters from orthogonal directions often exceeds one octave, potentially leading to instability in TF estimations using tensor processing techniques. Bastani and Pedersen (2001) proposed an enhanced impedance tensor estimation method based on a truncated singular value decomposition. A scalar, or univariate, estimation decouples the TFs in XY- and YX-polarizations and produces only off-diagonal impedance tensor elements Z_{xy} and Z_{yx}, while assuming the diagonal elements (Z_{xx} and Z_{yy}) in Equation (2) to be zero. This is a significant drawback in scalar techniques, as advanced data analyses techniques require full impedance tensor estimates. Moreover, scalar estimation assumes an idealized 2D subsurface condition, whereas tensor estimation incorporates full 3D subsurface information.

Despite advancements in the RMT method, scalar estimation remains widely applied in RMT data analysis. When using scalar estimation, TFs are estimated at a single site for two separate transmitter directions (aligned with the x- and y-axes), effectively increasing the number of frequencies analysed. Each transmitter has unique direction-dependent frequency content, enabling independent TF calculations for XY- and YX-polarizations. Tensor estimation is not common for RMT studies, as for accurate computation of the full impedance tensor, radio signals must meet strong criteria, including high S/N ratio,

sufficient coherency, appropriate azimuthal range and particularly similar signal frequencies in both polarizations simultaneously. Therefore, scalar processing usually provides more data because each polarization can be independently analysed using two orthogonally coupled fields that meet the necessary criteria.

Traditionally, scalar-estimated RMT data are evaluated predominantly with 2D inversion schemes. Newman et al. (2003) demonstrated that scalar-processed RMT data can be adapted for 3D inversion, enabling more realistic interpretation of subsurface structures. The 3D RMT inversion presented in this study uses a combination of scalar, tensor, and tipper data as input for the ModEM algorithm.

3.2 | Analysis of Scalar, Tensor and Tipper Data

To evaluate the quality and characteristics of scalar, tensor and tipper data, they are depicted in Figure 3 using different visualizations.

The apparent resistivity plotted for all soundings along profile 2 ranges roughly between 10 and 1000 Ω m, whereas the phase is mostly above 45° (Figure 3a–c). Few scattered data points are visible, which are omitted from subsequent inversion. A notable signal gap is visible between 40 and 300 kHz for scalar, tensor as well as tipper data. This gap is likely due to the remote survey location and possibly shadow effects from the Himalayan ridge, limiting the availability of transmitters in the LF range.

Figure 3d–f presents the data along profile 2 for the lowest (∼20 kHz) and highest (∼794 kHz) evaluated frequencies. We observe a few prominent features:

- The apparent resistivity slightly varies around 350 Ω m, and the phase is above 45° until profile meter 150.
- At ∼180 m along the profile line, an abrupt decrease in apparent resistivity from ∼350 to ∼35 Ω m appears. This feature is referred to as the 'conductivity contrast zone' in subsequent discussions. This trend is clearly visible in the scatter plots for scalar processing (Figure 3g) and less pronounced for the tensor data (Figure 3h).
- Further along the profile line, minor changes in apparent resistivity are observed, suggesting the presence of small-scale subsurface variations.
- Both polarizations compare well along major parts of the profile, indicating little multi-dimensional effects in the data. However, close to the conductivity contrast zone *XY*- and *YX*-polarization diverge slightly. This is particularly noticeable for the 20 kHz phase plot in Figure 3d.

The real and imaginary components of the tipper vector are plotted separately along the profile line in Figure 3f. Near the conductivity contrast zone, the real part of the tipper shows high values for both polarizations, caused by the lateral conductivity change. With increasing distance, the tipper vectors are either small, scattered or sparse, indicating a predominantly 1D resistivity distribution.

The color-coded apparent resistivity map in Figure 3g,h for 20 kHz highlights spatial conductivity variations. Particularly, the scalar data shows the transition zone as well as a second pronounced conductive structure further north. The amplitude of the tipper in Figure 3i clearly shows the multi-dimensional effects in the vicinity of the conductivity contrast zone.

3.3 | Comparison of Scalar and Tensor Data

Comparing the scalar and tensor data in Figure 3g,h demonstrates the major problem with tensor processing. Several stations are excluded due to low S/N ratio and poor coherency, leading to reduced data coverage compared to scalar processing. Additionally, tensor processing requires transmitters at the same or neighbouring frequencies for each polarization. However, this condition was not met for some stations and frequencies, resulting in reduced data density in the tensor-processed dataset. In total 43 stations have insufficient data quality for reliable tensor analysis, leading to gaps in the station distribution (cf. Figure 3h). These non-existent stations are masked in Figure 3g–i.

In situations where the subsurface resistivity distribution exhibits predominantly 1D or 2D characteristics, the impedance components derived from scalar and tensor estimations are theoretically similar. However, inverting scalar-processed data using a 3D framework can lead to misinterpretations, in case strong 3D effects are present. To be able to apply a 3D inversion scheme using a combination of scalar and tensor data, it is crucial to validate the consistency of both datasets. This ensures that scalar-based inversion remains viable, as 3D inversion algorithms typically compute the forward response as if the data has been processed using tensor estimation routines (Newman et al. 2003). Due to the poor coverage of our tensor processed RMT data, it is meaningful to combine it with the scalar-estimated data. The comparison between scalar and tensor estimated data along profile 2 and for a 20 kHz frequency in Figure 4 indicates only minor differences except for the conductivity contrast zone, rendering the combination of both datasets feasible.

The deviation between scalar and tensor data at approximately profile meter 180 in the phase curve plot highlights the presence of multi-dimensional subsurface features. Existing deviations between both estimates visible here, mainly in the *YX*-polarization indicate that an interpretation of scalar data using a 3D inversion algorithm can lead to misinterpretations. However, the comparison suggests that for large parts of the data, scalar estimates can be reliably used in a 3D inversion.

Newman et al. (2003) presented an analysis for using scalar-estimated RMT data in a 3D inversion framework. They demonstrated that scalar field data could be effectively analysed using tensor-based 3D inversion codes under the assumption that

$$\left|Z_{ji}\right| \gg \left|Z_{jj}P\right| \tag{6}$$

with P defined as

$$P = H_j/H_i \; i,j = \{x,y\} \tag{7}$$

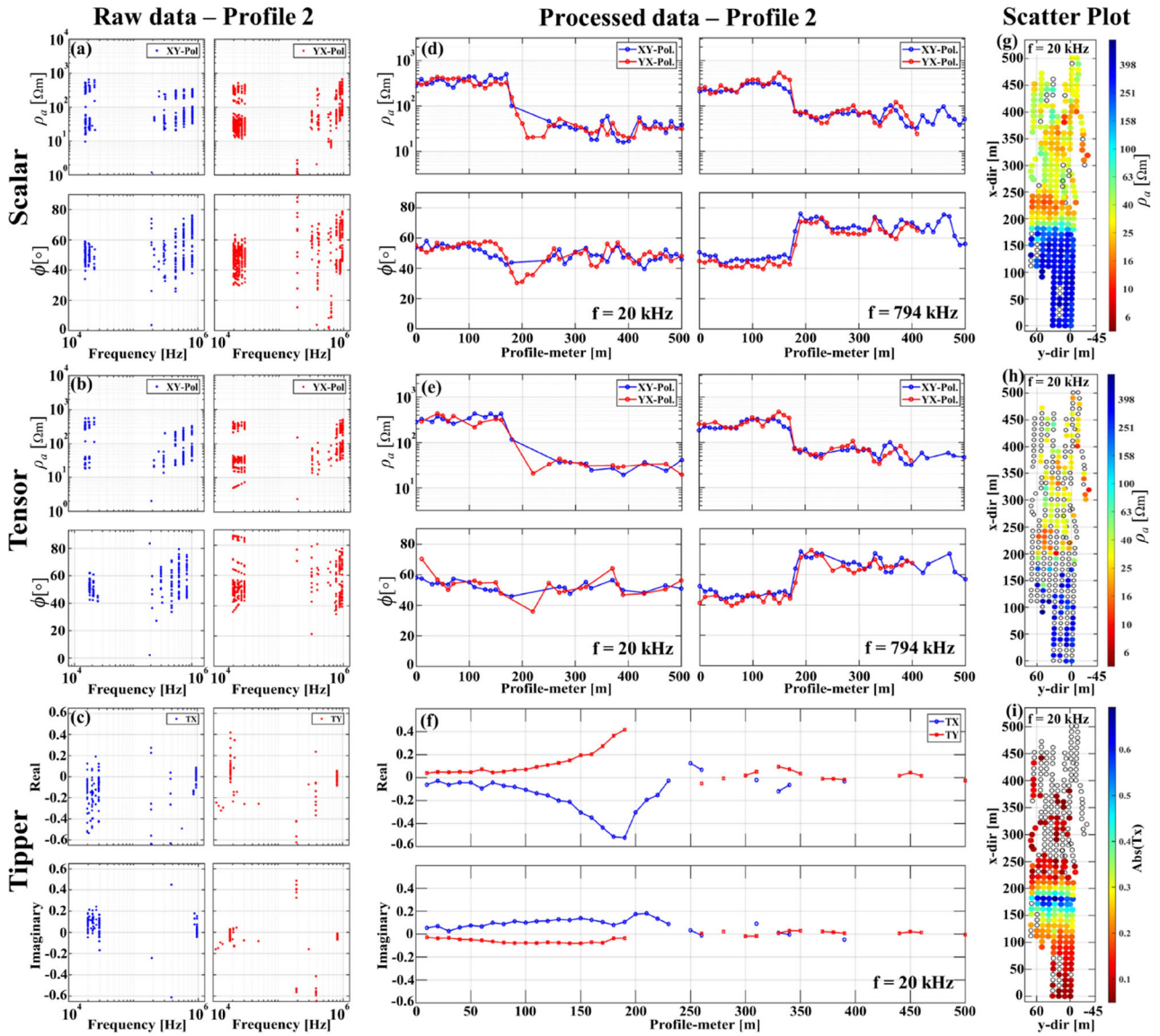

FIGURE 3 | Data shown exemplarily for profile 2. Raw data sounding curves for all stations along profile 2 for (a) scalar, (b) tensor, and (c) tipper processing. Processed (edited) data for two selected frequencies (20 and 794 kHz) along profile 2 for (d) scalar and (e) tensor processing. (f) Real and imaginary part of the tipper along profile 2 for a 20-kHz frequency. *E*-polarization scatter plots of the apparent resistivity for 20 kHz for (g) scalar and (h) tensor processing. (i) Scatter plot of the absolute value of the tipper (T_x).

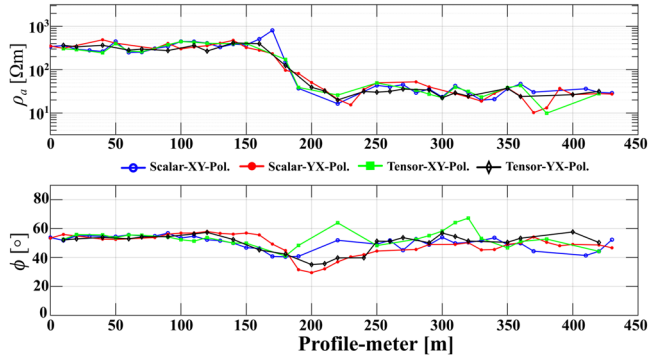

FIGURE 4 | Comparison between scalar and tensor estimated apparent resistivity and phase along profile 2 for an exemplary frequency of 20 kHz.

For a 2D conductivity distribution and a polarization of the electrical field in *j*-direction, H_j equals 0 and the criteria in Equation (6) is fulfilled. In this case the tensor-estimated off-diagonal elements equal the scalar estimation.

$$Z_{ij(\text{tensor})} \approx Z_{ij(\text{scalar})} \tag{8}$$

For a 3D conductivity distribution, P deviates from 0 and the validity of Equations (6) and (8) must be further evaluated.

Due to very noisy diagonal impedance components in the RMT dataset as well as varying frequency content in different polarizations, we use an approach alternative to Newman et al. (2003). Here we simply estimate the deviation between scalar and tensor off-diagonal elements to investigate the validity of using the full tensor approach implemented in the 3D inversion algorithm

TABLE 1 | Information about different data types with the amount and the percentages of available data.

Data types	No. of data	Percentage of full dataset	Component
Scalar	1469	48	Z_{xy}, Z_{yx}
Tensor (on/off-diagonal)	2109 (1063/1046)	35/34	Full Z
Tipper T	550	18	T_x, T_y
Combined (scalar, tensor and tipper)	3066 (1063, 1452, 550)	35, 47, 18	Z_{xy}, Z_{yx}, full Z, T_x, T_y

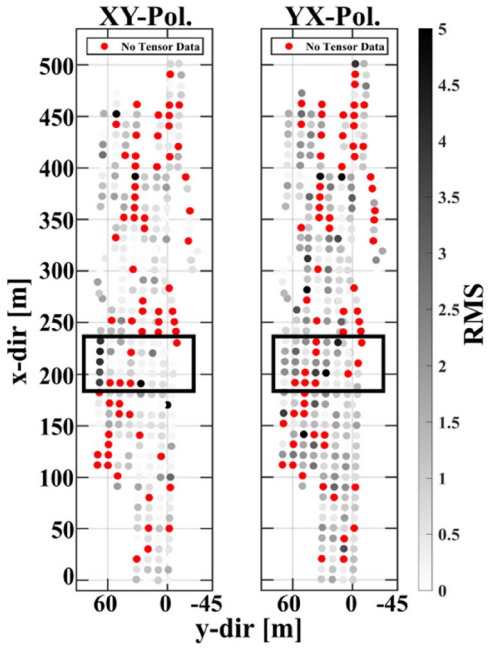

FIGURE 5 | Calculated RMS plotted as spatial map for the *XY*- and *YX*-polarization. The red dots indicate stations with missing tensor data. The transition zone is marked where the tensor data were not combined with scalar ones.

ModEM. Due to the comparably low S/N ratio in the tensor estimated data and, therefore, reduced number of usable tensor data, we adopt a hybrid approach combining scalar and tensor data to yield high data coverage. To ensure that the combined dataset fulfils the criterion of Equation (8), we calculate the error-weighted root mean square (RMS) between scalar and tensor data for both polarizations (see Figure 5). Sounding locations without any tensor data are marked red. We only include data from scalar estimates, if tensor and scalar data from stations surrounding the missing ones show a median RMS value below 2 in both polarizations. Except the transition zone marked in Figure 5 is not filled with scalar data, as systematic deviations are observed here. Particularly, the phase plot for the *YX*-polarization data in Figure 4 highlights those deviations. The large deviations in the *XY*-polarization. in the transition zone along profile 8 are likely caused by 3D effects, possibly related to the presence of outcrops in the station's vicinity. With this condition the tensor dataset is combined with scalar data using in total additional 407 off-diagonal data. Another approach based on estimating the skewness was also tested yet fails due to noisy diagonal components in the tensor data.

Table 1 gives an overview of the different available data types and the amount of data usable for inversion input, which significantly increases for the combined data.

3.4 | RMT 3D Inversion

Only very few 3D inversion studies exist for interpretation of high-frequency RMT data (e.g., Newman et al. 2003; Bastani et al. 2012; Fadavi Asghari et al. 2023). Our study employs the widely used 3D MT inversion algorithm ModEM (Egbert and Kelbert 2012) for high-frequency RMT data.

ModEM uses a finite difference forward calculation. The algorithm offers significant flexibility in inversion input parameter arrangements and allows the combination of different datasets. Additionally, its parallel computing framework effectively handles large memory and computational requirements for solving the forward and inverse problem.

A regularized inversion scheme is implemented, consisting of a penalty function that incorporates data misfit and model norm terms.

$$\phi(m,d) = \left(\bar{\mathbf{d}} - \bar{f}(\bar{\mathbf{m}})\right)^{\mathrm{T}} C_d^{-1} \left(\bar{\mathbf{d}} - \bar{f}(\bar{\mathbf{m}})\right) + \upsilon(\bar{\mathbf{m}} - \bar{m}_0)^{\mathrm{T}} C_m^{-1} (\bar{\mathbf{m}} - \bar{m}_0) \tag{9}$$

with model parameter vector $\bar{\mathbf{m}}$, and data vector $\bar{\mathbf{d}}$. $\bar{m}_0$ denotes a homogeneous starting model, C_d is the data co-variance matrix and C_m the model covariance matrix. $\overline{d'} = \bar{f}(\bar{\mathbf{m}})$ is the forward operator used to generate the response $\overline{d'}$. υ is as trade-off parameter between data closeness and model roughness.

To evaluate quality of the inversion results, we use the error-weighted RMS

$$\mathrm{RMS} = \sqrt{\frac{1}{N}\sum_{i=1}^{N} \frac{\left(\bar{d}_i - \bar{d}_i'\right)^2}{\delta \bar{d}_i^2}} \tag{10}$$

where $\delta \bar{d}_i^2$ is the error of the observed data.

This study presents the first application of ModEM to scalar- and tensor-estimated RMT field data, including tipper, within the frequency band of 10 kHz to 1 MHz. We include impedance tensor components together with the tipper vector. By using the tipper, the recovery of lateral conductivity variations can be improved (Tietze and Ritter 2013).

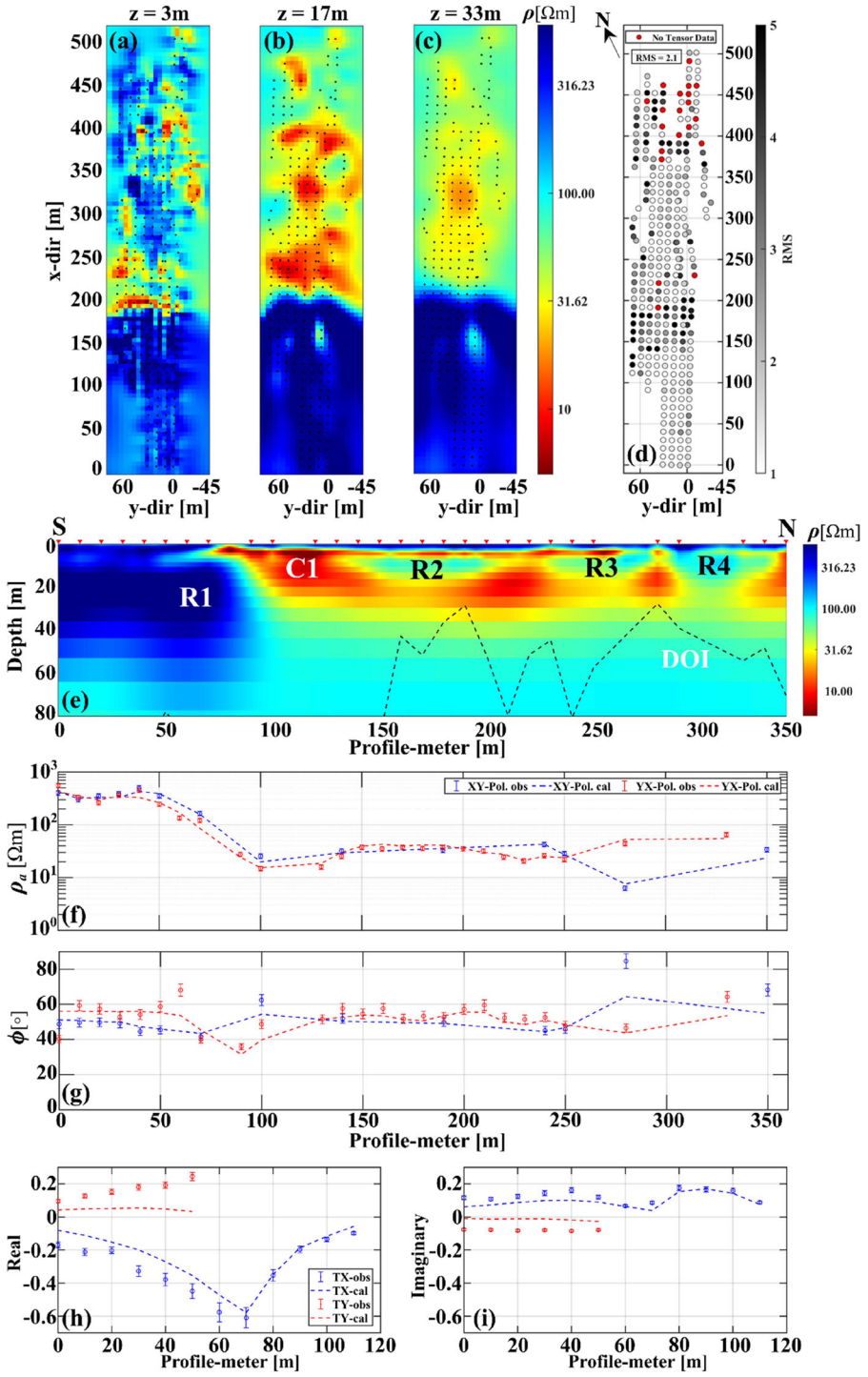

FIGURE 6 | The depth-section slices (for 1, 17 and 33 m) are derived from the 3D inversion of the combined (Sc/Ten+Tip) (a–c) dataset; (d) shows the colour-coded map of the distribution of RMS errors for the *XY*-pol., each red circle on the RMS plot shows stations unfilled with scalar data; (e) depicts an example cross-section plot derived from combined data for profile 5. The DOI is indicated by a dashed black line. R1, R2, R3 and R4 represent resistive structures, C1 is a conductor. The data fit plots for a selected frequency (20 kHz) are shown in panels (f) and (g). The former depicts the apparent resistivity, whereas the latter illustrates the phase of the off-diagonal elements. In both cases, blue circles represent the *XY*-polarization, whereas red circles correspond to the *YX*-polarization. Panels (h) and (i) show, respectively, real and imaginary parts of the tipper vector.

The ModEM inversion parameters, such as model discretization, starting model resistivity, data error bounds and regularization parameters, play a significant role in the 3D inversion and were carefully optimized. A homogeneous half-space starting model with a resistivity of 100 Ω m, derived from the apparent resistivity values, was used. The computational grid comprised 120 × 40 × 40 cells, with a horizontal cell size of 5 m in the main grid, increasing by a factor of 1.3 for 10 padding cells in lateral directions. The first layer thickness was set to 0.5 m, increasing by a factor of 1.2 with depth. The initial regularization parameter was set

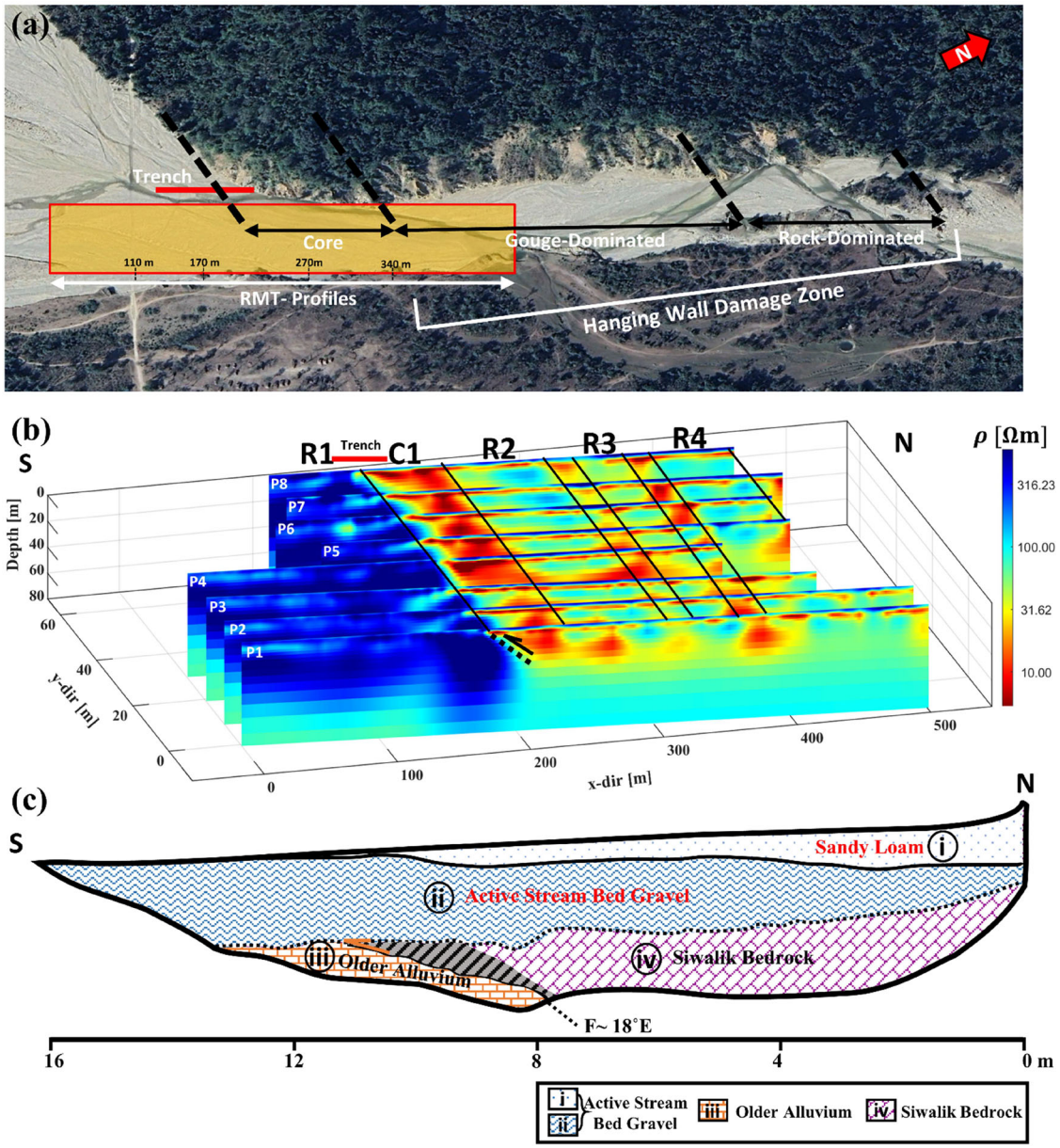

FIGURE 7 | (a) Conceptual model of the HFT fault zone (Srivastava et al. 2016). The survey area is marked in orange. The trench log (ZT-02) location is marked as red line. (b) 3D model view (SSW–NNE). (c) The trench model extends to a depth of 10 m and spans a width of 16 m. Geological formations are labelled (Kumar et al. 2006).

to 1, iteratively reduced by a factor of 10 during the inversion process (Kelbert et al. 2014). Additionally, a smoothing parameter of 0.3 was used for all directions, following the default setting in ModEM. Although a major issue in MT surveying and subsequent 3D modelling, static shift effects are rarely reported for the RMT method (e.g., Linde and Pedersen 2004). There are no obvious static shift effects observed in our RMT data.

4 | Results and Interpretation

The 3D inversion is performed using the combined dataset, as it offers superior data coverage. For the combined dataset, we integrated scalar data in the tensor data and included tipper estimations. This resulted in a combined dataset of 3066 data points (see Table 1). Overall, we added 407 off-diagonal scalar data. To account for potential errors due to geometry, device resolution and EM noise, an error floor of 5% of $|Z_{ij}|$ was set for off-diagonal components (Tietze and Ritter 2013; Meqbel et al. 2014). Diagonal components showed significantly smaller magnitudes, making them more prone to noise. To mitigate this, a down-weighting strategy was employed, assigning an error floor of 15% of $\sqrt{Z_{xy} \cdot Z_{xx}}$ for Z_{xx} and $\sqrt{Z_{yx} \cdot Z_{yy}}$ for Z_{yy}.

4.1 | Preferred 3D Inversion Result

Figure 6 depicts slice plane views of the 3D model at three different depths as well as an N–S resistivity depth section along

TABLE 2 | The resistivity and thickness values derived from the 3D model in Figure 7b and from the stratified geological formations described in the trench model in Figure 7c.

Geological formations	Modelled resistivity (Ωm)	Thickness (m)
(i) Sandy loam	~400	~2–4
(ii-south) Stream bed gravel	~200–350	~10
(ii-north) Stream bed gravel, wet, intermixed with clay	~5–20	~5–7
(iii) Older alluvial deposit	~400–600	~20–30
(iv) Siwalik bedrock	~10–35	—

profile 5 together with data and response plots. Few prominent features are evident:

- A resistive layer (>350 Ω m) is present in major parts of the shallow model section.
- Few more conductive structures (10–30 Ω m) are prominent in the northeastern part and close to the transition zone.
- The prominent conductivity contrast zone at $\sim x = 200$ m is spatially consistent across profiles and extends to greater depth.

The resistivity depth section along profile 5 in Figure 6e shows alternating major conductive and resistive zones. The most prominent lateral discontinuity is at around $\sim x = 70$ m between R1 and C1. C1, directly at the transition zone, extends to a depth of roughly 35 m covered by a ~2 m-thick resistive overburden. The lateral span is around ~30 m. At greater depth the conductor seems to extend laterally to roughly 265 m towards north. More resistive zones (R2, R3 and R4) seem to be embedded in a lens shaped manner into C1. The effective depth of investigation (DOI), estimated as approximately 1.5 times the skin depth (Spies 1989), is computed using $\mathrm{DOI} = 750 \times \sqrt{\rho_{\mathrm{ave}}/f_{\mathrm{min}}}$, where ρ_{ave} is the average resistivity of the model columns below each station, and f_{min} is the lowest frequency. For the conductive model section north of the transition zone, the DOI varies roughly between 40 and 60 m.

After 32 iterations, the global RMS improved from 7.65 to 2.01, reflecting overall well fitted data and sufficient convergence. The RMS values are below 5 across all stations, indicating a good match between observed data and model responses (Figure 6d). The data fit analysis in Figure 6e,f demonstrates good agreement between observed and calculated data along the profile for both impedance and tipper data. The good fit of both real and imaginary part of T_x and T_y support the reliability of the model.

Tensor processing routines compute the full impedance and theoretically offer a more comprehensive dataset for 3D interpretation. However, this does not exclude the use of scalar-estimated TFs for 3D inversions. The viability of scalar TFs depends on ensuring that both datasets have similar scales, a condition that our scalar data largely satisfies (see Figure 4). Using the ModEM 3D algorithm, we performed the inversion on a combined dataset, revealing conductive and resistive structures aligned along the profiles at relevant depths (Figure 6) leading to a largely consistent 3D model.

4.2 | Geological Interpretation

For an elaborate interpretation of the subsurface, we compare our preferred 3D model to the trench model (Figure 7b,c). Moreover, we discuss the model with respect to previous geological studies.

The fault core zone depicted in Figure 7a extends approximately 200 m along the RMT profiles (between $x = 150$ and 340 m). It consists of fine-grained gouges of Middle Siwalik rocks formed due to compression and deformation processes. Within this core zone, the derived 3D model depicts distinct alternating resistor-conductor patterns named C1, R2, R3 and R4. This structural variation compares well with visible outcrops composed of different rock types, influencing resistivity based on factors such as grain size, water saturation and clay content. For instance, the low resistivity values of C1 are likely to be associated with water-saturated clay and fine sand formations within the highly sheared and fractured core zone. The relatively high resistivity of R2 possibly reflects reduced clay content as well as reduced water content due to its lithological composition, although the gouge dominated zone is highly sheared and fractured, similar to the core zone (Srivastava et al. 2016). According to Srivastava et al. (2016), isolated resistive structures (such as R2) can limit fluid infiltration, whereas channelized zones (C1) enhance it. This underscores the role of water saturation in fault zones as a primary factor influencing resistivity variations.

Our preferred 3D model structure indicates strong agreement with the trench model, confirming the stratigraphic and structural interpretations given by Kumar et al. (2006). The trench model in Figure 7c depicts four main strata: (i) sandy loam, (ii) active stream bed gravel, (iii) older alluvium and (iv) the Siwalik bedrock. The top two layers (i and ii) are laterally continuous and overlay the discontinuous formations (iii) and (iv). Note that the trench study and the RMT survey were conducted in different years and seasons, and they are not exactly co-located, limiting a robust comparison. Moreover, the survey area is located within the Solani River's north–south flow direction. Therefore, sedimentation is seasonally dependent and actively driven by material transport and/or accumulation. These fluvial processes play a dominant role in forming stratigraphic units, such as the active stream bed gravel or the top surface sandy loam layer.

Interpreting the area by dividing it into two distinct regions (southern from $x = 0$–200 m and central core zone $x = 200$–250 m) is beneficial for discussing the stratigraphic and lithological characteristics, as well as determining resistivity and thickness ranges (cf. Table 2).

According to the trench model in Figure 7c, the active stream bed gravel (ii) overlays the complete survey area, whereas the sandy loam layer (i) is intersected midway along the trench.

In the northern zone, we observe a thin resistor (~400 Ω m) at the surface that we interpret as sandy loam (i), followed by saturated active stream bed gravel intermixed with clays, most likely from the Siwalik lowering the resistivity values to ~5–20 Ω m (ii-north). The oldest exposed unit in the trench model is the highly sheared and fractured Siwalik bedrock (iv). This formation is designated as C1 in the resistivity model, characterized by a low resistivity of 10–35 Ω m that can be traced down to ~40 m depth (max DOI). The low resistivity values are attributed to the presence of saturated clayey and fine sand formations within the fractured bedrock.

The southern zone (x = 0–200 m) corresponds to the R1 unit in the resistivity model (Figure 7b). This unit represents a rather uniform high-resistive medium. According to the trench, the active stream bed gravel (ii-south) is followed by the older alluvium (iii) at depth, which is resistive with 400–600 Ω m. However, in the southern zone, clay minerals are likely to be completely washed out from the active stream bed gravel—leading to comparably high resistivity values with 200–350 Ω m (ii-south). In order to avoid possible misinterpretation, we do not interpret any internal layering within R1, although some variations within the upper 40 m are observed that might be related to the stratigraphic units or also tectonic processes close to the core zone. As an inductive method, RMT is limited in resolving small variations within resistive environments.

A prominent attribute is the conductivity contrast zone (R1/C1), which is interpreted as the interface where the Siwalik bedrock (iv) overrides the alluvial deposits (iii). This interface likely corresponds to a low-angle (~20°–30°) thrust fault, designated as F1 in the trench model, highlighting the tectonic and sedimentary interactions shaping the region. We identified an angle of roughly 30° in our derived models.

5 | Conclusion

Here, we present a 3D inversion study of RMT data obtained in the Sub-Himalayan region near Mohand, India. The derived 3D conductivity model successfully correlates the surface manifestations of the HFT fault with a shallow conductivity contrast zone.

The RMT data, collected at 312 sites in a frequency range between ~20 and 794 kHz exhibit high data quality at most sites. Due to the limited accessibility of transmitters with different polarizations in a shared frequency range, RMT data are conventionally processed with a scalar approach and further analysed in 2D. In this study, we combined scalar, tensor and tipper data to utilize the advantage of complementary information from the full impedance tensor and vertical magnetic field data.

With the application of an RMS criterion for the inclusion of scalar data from regions with a preliminary 2D conductivity distribution into the tensor dataset, we ensure the applicability of ModEM for 3D inversion. Due to the high data coverage, the combined RMT dataset produces a robust 3D conductivity model with good data fit.

The resulting 3D model consistently depicted a sharp conductivity contrast with a uniform elongation direction across all profiles. These models corroborate the geological structures identified in previous studies, successfully correlating the surface manifestation of the HFT fault with the conductivity contrast zone. This zone delineates the steep boundary between the Siwalik bedrock and alluvial deposits. Distinct formations within the core zone were traceable, with their unique material compositions reflected in their resistivity values. These findings demonstrate the efficacy of the RMT method in tracing emergent faults at shallow depths, making it a valuable tool for geophysical investigations in tectonically active regions.

Acknowledgements

This work was conducted as part of the INDO-GERMAN joint research collaboration under the DST-DAAD project (Project No. DST/INT/DAAD/P-19/2019 - TPN 73918; DAAD No. 57622770). We gratefully acknowledge the financial support provided by the funding agencies (DST and DAAD). Additionally, we extend our sincere appreciation to the anonymous reviewers and editors for their valuable comments, which have contributed to the improvement of this manuscript.

Data Availability Statement

The data that support the findings of this study are available from the corresponding author upon reasonable request.

References

Bastani, M., J. Hübert, T. Kalscheuer, L. B. Pedersen, A. Godio, and J. Bernard. 2012. "2D Joint Inversion of RMT and ERT Data Versus Individual 3D Inversion of Full Tensor RMT Data: An Example From Trecate Site in Italy." *Geophysics* 77, no. 4: WB233–WB243. https://doi.org/10.1190/GEO2011-0525.1.

Bastani, M., and L. B. Pedersen. 2001. "Estimation of Magnetotelluric Transfer Functions From Radio Transmitters." *Geophysics* 66, no. 4: 1038–1051. https://doi.org/10.1190/1.1487051.

Bastani, M., A. Savvaidis, L. B. Pedersen, and T. Kalscheuer. 2011. "CSRMT Measurements in the Frequency Range of 1–250 kHz to Map a Normal Fault in the Volvi Basin, Greece." *Journal of Applied Geophysics* 75, no. 2: 180–195. https://doi.org/10.1016/J.JAPPGEO.2011.07.001.

Cagniard, L. 1953. "Basic Theory of the Magneto-Telluric Method of Geophysical Prospecting." *Geophysics* 18, no. 3: 605–635. https://doi.org/10.1190/1.1437915.

Candansayar, M. E., and B. Tezkan. 2008. "Two-Dimensional Joint Inversion of Radiomagnetotelluric and Direct Current Resistivity Data." *Geophysical Prospecting* 56 no. 5: 737–749. https://doi.org/10.1111/J.1365-2478.2008.00695.X.

Cantwell, T. 1960. "Detection and Analysis of Low Frequency Magnetotelluric Signals." Doctoral diss., Massachusetts Institute of Technology.

Devi, A., M. Israil, A. Singh, P. K. Gupta, P. Yogeshwar, and B. Tezkan. 2020. "Imaging of Groundwater Contamination Using 3D Joint Inversion of Electrical Resistivity Tomography and Radio Magnetotelluric Data: A Case Study From Northern India." *Near Surface Geophysics* 18, no. 3: 261–274. https://doi.org/10.1002/NSG.12092.

Egbert, G. D., and J. R. Booker. 1986. "Robust Estimation of Geomagnetic Transfer Functions." *Geophysical Journal International* 87, no. 1: 173–194. https://doi.org/10.1111/J.1365-246X.1986.TB04552.X.

Egbert, G. D., and A. Kelbert. 2012. "Computational Recipes for Electromagnetic Inverse Problems." *Geophysical Journal International* 189, no. 1: 251–267. https://doi.org/10.1111/J.1365-246X.2011.05347.X/3/189-1-251.

Fadavi Asghari, S., A. Shlykov, M. Smirnova, A. Saraev, P. Yogeshwar, and B. Tezkan. 2023. "Multidimensional Interpretation of Radiomagnetotellurics and Controlled-Source Radiomagnetotellurics Data: A Validation Study." *Near Surface Geophysics* 21, no. 4: 300–313. https://doi.org/10.1002/nsg.12257.

Farquharson, C. G., D. W. Oldenburg, E. Haber, and R. Shekhtman. 2002. "An Algorithm for the Three-Dimensional Inversion of Magnetotelluric Data." *SEG Technical Program Expanded Abstracts* 2002: 649–652. https://doi.org/10.1190/1.1817336.

Gamble, T. D., W. M. Goubau, and J. Clarke. 1979. "Magnetotellurics With a Remote Magnetic Reference." *Geophysics* 44: 53–68.

Goldstein, M. A., and D. W. Strangway 1975. "Audio-Frequency Magnetotellurics With a Grounded Electric Dipole Source." *Geophysics* 40, no. 4: 669–683. https://doi.org/10.1190/1.1440558.

Grayver, A. V. 2015. "Parallel Three-Dimensional Magnetotelluric Inversion Using Adaptive Finite-Element Method. Part I: Theory and Synthetic Study." *Geophysical Journal International* 202, no. 1: 584–603. https://doi.org/10.1093/GJI/GGV165.

Israil, M., D. K. Tyagi, P. K. Gupta, and S. Niwas. 2008. "Magnetotelluric Investigations for Imaging Electrical Structure of Garhwal Himalayan corridor, Uttarakhand, India." *Journal of Earth System Science* 117, no. 3: 189–200. https://doi.org/10.1007/S12040-008-0023-0/METRICS.

Kelbert, A., N. Meqbel, G. D. Egbert, and K. Tandon. 2014. "ModEM: A Modular System for Inversion of Electromagnetic Geophysical Data." *Computers & Geosciences* 66: 40–53. https://doi.org/10.1016/J.CAGEO.2014.01.010.

Kumar, S., S. G. Wesnousky, R. Jayangondaperumal, T. Nakata, Y. Kumahara, and V. Singh. 2010. "Paleoseismological Evidence of Surface Faulting Along the Northeastern Himalayan front, India: Timing, Size, and Spatial Extent of Great Earthquakes." *Journal of Geophysical Research: Solid Earth* 115, no. B12. https://doi.org/10.1029/2009JB006789.

Kumar, S., S. G. Wesnousky, T. K. Rockwell, R. W. Briggs, V. C. Thakur, and R. Jayangondaperumal. 2006. "Paleoseismic Evidence of Great Surface Rupture Earthquakes Along the Indian Himalaya." *Journal of Geophysical Research: Solid Earth* 111, no. B3: 3304. https://doi.org/10.1029/2004JB003309.

Le Fort, P. 1975. "Himalayas: The Collided Range. Present Knowledge of the Continental Arc." *American Journal of Science* 275: 1–44.

Linde, N., and L. B. Pedersen. 2004. "Characterization of a Fractured Granite Using Radiomagnetotelluric (RMT) Data." *Geophysics* 69, no. 5: 1155–1165. https://doi.org/10.1190/1.1801933.

Malehmir, A., M. Andersson, S. Mehta, et al. 2016. "Post-Glacial Reactivation of the Bollnäs fault, central Sweden—A Multidisciplinary Geophysical Investigation." *Solid Earth* 7, no. 2: 509–527. https://doi.org/10.5194/SE-7-509-2016.

Meqbel, N. M., G. D. Egbert, P. E. Wannamaker, A. Kelbert, and A. Schultz. 2014. "Deep Electrical Resistivity Structure of the Northwestern U.S. Derived From 3-D Inversion of USArray Magnetotelluric Data." *Earth and Planetary Science Letters* 402, no. C: 290–304. https://doi.org/10.1016/J.EPSL.2013.12.026.

Miglani, R., M. Shahrukh, M. Israil, P. K. Gupta, S. K. Varshney, and S. Elena. 2014. "Geoelectric Structure Estimated From Magnetotelluric Data From the Uttarakhand Himalaya, India." *Journal of Earth System Science* 123, no. 8: 1907–1918. https://doi.org/10.1007/S12040-014-0504-2.

Molnar, P. 1990. "A Review of the Seismicity and the Rate of Active Underthrusting and Deformation at the Himalaya." *Journal of Himalayan Geology* 1, no. 2: 131–154.

Newman, G. A., S. Recher, B. Tezkan, and F. M. Neubauer. 2003. "3D Inversion of a Scalar Radio Magnetotelluric Field Data Set." *Geophysics* 68, no. 3: 791–802. https://doi.org/10.1190/1.1581032.

Pedersen, L. B. 1982. "The Magnetotelluric Impedance Tensor—Its Random and Bias Errors." *Geophysical Prospecting* 30, no. 2: 188–210. https://doi.org/10.1111/j.1365-2478.1982.tb01298.x.

Pedersen, L. B., M. Bastani, and L. Dynesius. 2006. "Some Characteristics of the Electromagnetic Field From Radio Transmitters in Europe." *Geophysics* 71, no. 6: G279–G284. https://doi.org/10.1190/1.2349222.

Raiverman, V., A. Mukerjea, M. K. Saproo, S. V. Kunte, and J. Ram. 1990. *Geological Map of Himalayan Foothills Between Yamuna and Sarda Rivers*. Keshava Deva Malaviya Institute of Petrolium Exploration, Oil and Natural Gas Corporation.

Rajendran, C. P., B. John, and K. Rajendran. 2015. "Medieval Pulse of Great Earthquakes in the Central Himalaya: Viewing Past Activities on the Frontal Thrust." *Journal of Geophysical Research: Solid Earth* 120, no. 3: 1623–1641. https://doi.org/10.1002/2014JB011015.

Saraev, A., A. Simakov, A. Shlykov, and B. Tezkan. 2017. "Controlled Source Radiomagnetotellurics: A Tool for Near Surface Investigations in Remote Regions." *Journal of Applied Geophysics* 146: 228–237. https://doi.org/10.1016/J.JAPPGEO.2017.09.017.

Shlykov, A. 2018. *EMP: Electromagnetic Processor*. https://www.csrmt.info.

Smirnova, M., A. Shlykov, S. Fadavi Asghari, et al. 2023. "3D Controlled-Source Electromagnetic Inversion in the Radio-Frequency Band." *Geophysics* 88, no. 1: E1–E12. https://doi.org/10.1190/geo2021-0626.1.

Spies, B. R. 1989. "Depth of Investigation in Electromagnetic Sounding Methods." *Geophysics* 54, no. 7: 872–888. https://doi.org/10.1190/1.1442716.

Srivastava, V., M. Mukul, and J. B. Barnes. 2016. "Main Frontal Thrust Deformation and Topographic Growth of the Mohand Range, Northwest Himalaya." *Journal of Structural Geology* 93: 131–148. https://doi.org/10.1016/J.JSG.2016.10.009.

Tezkan, B. 1999. "A Review of Environmental Applications of Quasi-Stationary Electromagnetic Techniques." *Surveys in Geophysics* 20, no. 3–4: 279–308. https://doi.org/10.1023/A:1006669218545.

Tezkan, B. 2009. "Radiomagnetotellurics." In *Groundwater Geophysics*. Springer. https://doi.org/10.1007/978-3-540-88405-7_10.

Widodo, and Tezkan, B. 2015. "Analysis of the Shallow Structures of Active Fault Zones Using 3D Radiomagnetotelluric Data Set." *Procedia Earth and Planetary Science* 12: 68–76. https://doi.org/10.1016/J.PROEPS.2015.03.037.

Tezkan, B., A. Hördt, and M. Gobashy. 2000. "Two-Dimensional Radiomagnetotelluric Investigation of Industrial and Domestic Waste Sites in Germany." *Journal of Applied Geophysics* 44, no. 2–3: 237–256. https://doi.org/10.1016/S0926-9851(99)00014-2.

Tezkan, B., I. Muttaqien, and A. Saraev. 2019. "Mapping of Buried Faults Using the 2D Modelling of Far-Field Controlled Source Radiomagnetotelluric Data." *Pure and Applied Geophysics* 176, no. 2: 751–766. https://doi.org/10.1007/S00024-018-1980-0.

Tezkan, B., and A. Saraev. 2008. "A New Broadband Radiomagnetotelluric Instrument: Applications to near Surface Investigations." *Near Surface Geophysics* 6, no. 4: 245–252. https://doi.org/10.3997/1873-0604.2008019.

Thakur, V. C. 2013. "Active Tectonics of Himalayan Frontal Fault System." *International Journal of Earth Sciences* 102, no. 7: 1791–1810. https://doi.org/10.1007/S00531-013-0891-7.

Thakur, V. C., and A. K. Pandey. 2004. "Active Deformation of Himalayan Frontal Thrust and Piedmont Zone South of Dehradun in Respect of Seismotectonics of Garhwal Himalaya." *Himalayan Geology* 25, no. 1: 23–31.

Tietze, K., and O. Ritter. 2013. "Three-Dimensional Magnetotelluric Inversion in Practice-the Electrical Conductivity Structure of the San Andreas Fault in Central California." *Geophysical Journal International* 195, no. 1: 130–147. https://doi.org/10.1093/GJI/GGT234.

Turberg, P., I. Müller, and F. Flury. 1994. "Hydrogeological Investigation of Porous Environments by Radio Magnetotelluric-Resistivity

(RMT-R 12–240 kHz).” *Journal of Applied Geophysics* 31, no. 1–4: 133–143. https://doi.org/10.1016/0926-9851(94)90052-3.

Unsworth, M. J., A. G. Jones, W. Wei, et al. 2005. “Crustal Rheology of the Himalaya and Southern Tibet Inferred From Magnetotelluric Data.” *Nature* 438, no. 7064: 78–81. https://doi.org/10.1038/nature04154.

Valdiya, K. S. 1973. “Tectonic Framework of India: A Review and Interpretation of Recent Structural and Tectonic Studies.” *Geophysical Research Bulletin* 11 79–114.

Verma, G. S. 1974. “Structure of the Foot-Hills of the Himalayas.” *Pure and Applied Geophysics Pageoph* 112, no. 1: 18–26. https://doi.org/10.1007/BF00875913/METRICS.

Vozoff, K. 1972. “The Magnetotelluric Method in the Exploration of Sedimentary Basins.” *Geophysics* 37, no. 1: 98–141. https://doi.org/10.1190/1.1440255.

Wesnousky, S. G., S. Kumar, R. Mohindra, and V. C. Thakur. 1999. “Uplift and Convergence Along the Himalayan Frontal Thrust of India.” *Tectonics* 18, no. 6: 967–976. https://doi.org/10.1029/1999TC900026.

Yeats, R. S., and V. C. Thakur. 2008. “Active Faulting South of the Himalayan Front: Establishing a New Plate Boundary.” *Tectonophysics* 453, no. 1–4: 63–73. https://doi.org/10.1016/j.tecto.2007.06.017.

Yogeshwar, P., B. Tezkan, M. Israil, and M. E. Candansayar. 2012. “Groundwater Contamination in the Roorkee Area, India: 2D Joint Inversion of Radiomagnetotelluric and Direct Current Resistivity Data.” *Journal of Applied Geophysics* 76: 127–135. https://doi.org/10.1016/j.jappgeo.2011.11.001.